AXSTRAN : A Non-LTE Radiation Transport and Ionization Dynamics Code in Axisymmetric Two-Dimensional Geometry

Y. K. Chong, T. Kammash and J. Davis*

Dept. of Nuclear Engineering, University of Michigan, Ann Arbor, MI 48109
**Radiation Hydrodynamics Branch, Naval Research Laboratory, Washington, DC 20375*

Abstract. A description of AXSTRAN, a fully coupled time-dependent non-LTE radiation ionization dynamics code with the nonlocal opacity effects and the radiation transport for axisymmetric 2-D geometry, is presented. A demonstration of the capability of the code is made through an examination of the radiation field and the ionization state in a finite uniform argon Z-pinch plasma.

I Introduction

Numerous one-dimensional theoretical investigations of hot dense Z-pinch and laser produced plasmas have shown that the radiation plays an important role in affecting the dynamics of the plasmas through an array of emission, nonlocal absorption and energy transfer processes which depend sensitively on the details of the ionization dynamics as well as the temperature, density and size of the plasmas.[1] These plasmas, however, are known to be subject to various sources of multidimensional nonuniformities and inhomogenieties such as the Rayleigh Taylor and MHD instabilities and boundary effects which affect strongly the property of the radiation field as well as the plasma dynamics. In order to accurately predict and understand the nonlinear coupling physics of the plasma and radiation ensemble, therefore, a self-consistent theoretical approach within a full multidimensional framework is required. In this paper, we present a description of AXSTRAN, a fully coupled detailed configuration, time-dependent non-LTE radiation ionization dynamics code with the nonlocal opacity effects and the radiation transport for axisymmetric (r,z) geometry. AXSTRAN can be used as a radiation ionization dynamics postprocessor, and has an appropriate module for efficient coupling to PRISM,[2] the two-dimensional Lagrangian MHD code at the Naval Research Laboratory, for detailed simulations of the dynamic evolution of a hot dense plasma. An application of the code is made by examining a n argon Z-pinch plasma.

II Model

In AXSTRAN, the determination of the radiation field and ionization states that are consistent with the temperature and density at each point in the plasma is achieved through the simultaneous solutions of the ionization dynamics (ID) or rate equations for the atomic level populations together with the radiative transfer equation (RTE) for the specific intensity of the radiation field in conjunction with the equations of state (EOS). An iterative solution technique is employed together with a number of acceleration techniques to facilitate the solution process. The electron and ion temperatures, which are related to the electron and ion specific internal energy densities and the ionization energy density, are determined from the ideal gas EOS. The effective charge $\bar{Z}$ and electron

CP409, *Dense Z-Pinches*: Fourth International Conference
edited by N. R. Pereira, J. Davis, and P. E. Pulsifer

density of the plasma are determined from the charge neutrality condition. The coupling of AXSTRAN to PRISM is made through the EOS and through the electron energy equation by the radiative power density. Furthermore, various transport coefficients in the MHD equations are affected by the internal ionization states.

The rate equation for the population density n_i of atomic level i may be written

$$\frac{dn_i}{dt} = \sum_{j \neq i} (W_{ij} n_j - W_{ji} n_i), \tag{1}$$

where W_{ij} is the total (collisional and radiative) transition rate coefficient from an arbitrary atomic level j to level i, and the sum is taken over all levels j with a direct transition to level i. An equation of this type is written for each atomic level i included in the atomic model. The atomic and radiative processes considered through a multilevel detailed configuration atomic model are: collisional ionization, photoionization, collisional, dielectronic and radiative (including stimulated) recombinations as well as collisional excitation and deexcitation, spontaneous and stimulated emissions and photoexcitation. The atomic data as well as the collisional rate coefficients are obtained according to the techniques outlined in Duston and Davis.[3] Unless the plasma is optically thin for which the radiation does not affect the levels, the evaluation of the radiative rate coefficients requires the specific intensity of the radiation from the solutions of the RTE. The solutions of Eq. (1) are obtained through a single-step time integration of an implicit integral representation of the equation that is derived from successive substitutions of the formation solution with appropriate closure schemes. Preliminary studies indicated that the method is superior in terms of accuracy and computer cost over the NRL method[4] without the limitation on the timestep. Under the collisional radiative equilibrium (CRE), the explicit time dependent term in Eq. (1) can be dropped and the standard decoupling technique is invoked for the equilibrium solution.

Because the radiation in a multidimensional hot dense plasma can be highly anisotropic and nonuniform (particularly near the optically thin outer region and in strong temperature or density gradient regions) with a strong and complex frequency dependence arising from its typical non-Planckian nature, the accurate description of the field requires, in general, a multifrequency multidirectional radiation transport with sufficient spectral and angular resolutions. In AXSTRAN, this is accomplished through the solutions of an appropriate form of the RTE which may be written in terms of the radiation specific intensity, I_ν, as[5]

$$\left[\sin\theta\cos\phi\frac{\partial}{\partial r} - \frac{\sin\theta\sin\phi}{r}\frac{\partial}{\partial\phi} + \cos\theta\frac{\partial}{\partial z}\right] I_\nu(r,z,\theta,\phi) = -\kappa_\nu(r,z) I_\nu(r,z,\theta,\phi) + j_\nu(r,z), \tag{2}$$

where the local radiative emission and absorption processes are represented by the total volume emission coefficient or emissivity, j_ν, and the opacity, respectively, κ_ν. The dominant radiative processes include the bound-bound (b-b), bound-free (b-f) and free-free (f-f) processes (and the inner-shell (IS) photoionization for higher energy photons in a cool dense plasma). Thus, j_ν and κ_ν can be represented by the sum of their respective contributions (including the stimulation contributions), and are determined from the atomic level populations and $\bar{Z}$ as well as the temperature and density. The spectral lines are modeled through Voigt profile under the assumption of complete frequency redistribution and whose broadening parameter includes all collisional and radiative processes affecting the upper and lower levels of each transition. The IS opacity is

incorporated using the technique prescribed in Duston, et al.[6]

The multifrequency discrete ordinates transport methodology is applied to the RTE. Separate adaptive frequency grid techniques are implemented to the lines, edges and continuum radiation in order to take into account the differences in their frequency variation, and with a sufficient grid resolution to differentiate the underlying physics and their overlapping. A Riemann sum quadrature formula is used for the integration of the frequency variable due to the highly nonuniform mesh, and for the angle domain, the double-Gauss quadrature formula,[7] with a position dependent quadrature order $N_\Omega(r,z)$ is employed. The angular quadrature set can be tailored to accommodate the nonuniform anisotropy of the radiation field. The resulting multifrequency discrete ordinate form of the RTE is solved using the accurate ray-based transport technique where the intensity of the rays are obtained by integrating the RTE along each ray characteristic. This requires complex and time-consuming three-dimensional geometric tracking of the rays through the plasma, and a suite of ray transport models are developed; each tailored to meet simultaneously the accuracy requirement of a particular problem and the computer CPU time and storage constraint.[8] In addition, a number of schemes such as the line-doubling and dynamic frequency resolution (dynamical variation of the frequency mesh such as to maintain the desired frequency resolution with the minimum number of frequency points at each iteration step) techniques are employed to speed the transport calculation.

III Application

The code was used for a detailed analysis of the radiation and ionization physics in an isodense isothermal argon Z-pinch plasma of 3.0 cm in length and 0.5 cm radius. It has 1 keV temperature and two ion density cases: 10^{19} and 10^{21} ions/cm^3 were considered. At this parameter regime, the plasma has $\bar{Z}$ of about 16, and we expect it to be collisionally dominated at 10^{21} density while the radiation to play a more significant role at the lower density. The plasma was taken to be in CRE and the electron and ion were assumed to be in thermal equilibrium. The argon atomic model included all 19 ground states and a total of 106 excited levels (chosen based on their energetic and diagnostic significance in balance with the computational cost) distributed more or less uniformly over the H-like Ar XVIII to Na-like Ar VIII ion stages. The transport calculations included a total of 77 b-b lines (seven per ionization stage from the Ar XVIII to Ar VIII consisting mainly of those arising from the transitions between ground states and low lying excited states) in addition to all 124 b-f edges and f-f continuum.

The plasma at 10^{19} density is moderately opaque to lines (κ_ν of the majority of the K- and L-shell lines is in the range of 10 -100 cm^{-1}) and quite transparent to continuum, while at 10^{21}, the lines become extremely optically thick (κ_ν of up to 10^4 cm^{-1}) and the continuum moderate to relatively thick. The source function, $S_\nu = j_\nu / \kappa_\nu$, at the plasma center as a function of photon energy is plotted in Fig. (1) for both densities. The local Planck function, B_ν, is shown by the dotted curve and would represent S_ν for an optically thick collisional LTE plasma. We observe for both densities that S_ν is essentially blackbody at lower energies, where the f-f processes dominate, but substantially below B_ν at higher energies, where the b-f processes persist. S_ν at the regions represented by the lines shows a much greater departure from B_ν than the surrounding continuum even though the lines are much more opaque. This arises as the local ionization state is affected by not only the opacity but also by the completing collisional processes. The higher energy K-shell radiation falls further from B_ν than the L-shell radiation as the K-shell transition levels are more likely to deviate from the LTE state due to their greater energy

separations and hence smaller collisional rates. Finally, S_ν at 10^{21} density is closer to B_ν (by about two orders of magnitude for the K-shell edges, for example) than at 10^{19} density as the higher collisional rates and opacity help the plasma toward LTE.

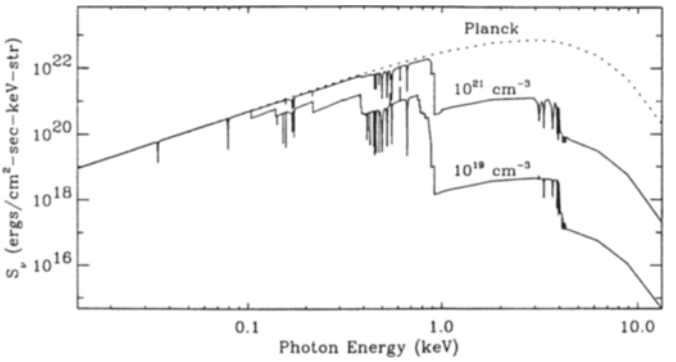

Fig. 1. S_ν at the plasma center at 10^{19} and 10^{21} densities. Planck function is shown by the dotted curve.

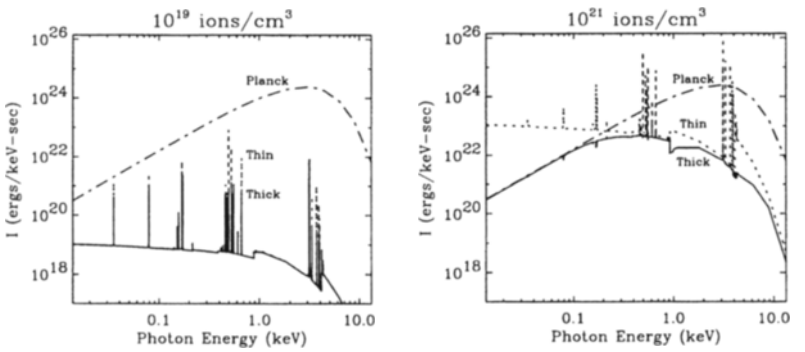

Fig. 2 Total volume integrated emission spectra (thick and thin) for both ion density cases. Blackbody emission curve is also shown for both cases.

The corresponding volume integrated total emission spectra are presented by the solid line curves in Fig. 2 with the blackbody emission limit being represented by the dash-dotted curves. The dotted line curves correspond to the results obtained under the optically thin approximation. The spectrum at 10^{19} density is dominated by lines with many of the K- and L-shell lines exhibiting a noticeable and in few cases substantial intensity decrease from their thin value while continuum is virtually unchanged. The spectrum at 10^{21} density, on the other hand, shows that the lines have virtually diminished down to the continuum level or reversed, leaving the continuum (although being substantially attenuated for the higher energy edges and the f-f radiation at lower energies) as the main contributor. The greater attenuation of the radiation at 10^{21} density is due to the increases in the radiation trapping and collisional quenching (thermalization

of photons by collisional rather than by radiative decays of the upper transition state). Relative to the Planck spectrum, we observe that although the spectrum at 10^{21} density is much closer to the blackbody curve in value and shape than at 10^{19} density, it differ markedly from B_ν throughout much of the energy range (E > 0.2 keV) due to the reasons stated earlier.

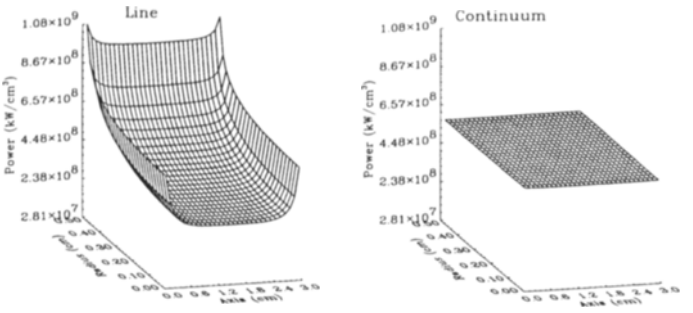

Fig. 3 Line and continuum radiative power densities (kW/cm^3) for 10^{19} density case.

The effects of the nonlocal opacity and transport on the property of the radiation field can be seen in Fig. (3) which presents surface plots of the line and continuum radiative power densities at 10^{19} ions/cm^3. We first observe that the continuum power density profile is practically uniform and flat throughout as the plasma is transparent to the continuum radiation. The line power, on the other hand, is significantly affected by the radiation transport and boundary effects as it is associated with a decrease at the optically thick interior regions and a substantial gradient that increases rapidly toward the optically thin surface regions where the photons are most likely to escape. This is compared to the line specific intensity which is uniform and isotropic in the inner plasma and decreases toward the plasma surface with increasing gradient and anisotropy.

Finally, in Fig. 4 are presented surface plots of the ratio of the optically thick over thin population densities of selected ground states at 10^{19} ions/cm^3 We observe that in addition to affecting the atomic levels via photopumping, the radiation have also introduced varying degrees of spatial nonuniformity to the level populations. The induced gradients in the level populations then act as an additional feedback mechanism to the radiation field gradients. We expect, for a given transition, the upper level population to be enhanced by photopumping while the lower level to become depleted, with a greater enhancement/depletion effect at the plasma center than at the surface. The figure shows that the Ar XVIII ground state (G) is photo-enhanced through out with the peak ratio of 1.134 at the plasma center, while the Ar XVII G is photo-depleted with the minimum ratio of 0.991 at the center and with an inverted ratio profile. The most interesting case occurs for the Ar XIII G Which undergoes the transition between photo-depleted to photo-enhanced stages from the plasma surface to the inner region. The Ar XII G is mildly affected by radiation. Since the b-f radiation is optically thin, we note that the photoionization has virtually no influence on the ground state populations. Thus, the most likely process by which the radiation affects the states is the cascade ionization (photoexcitation of the excited levels followed by collisional ionization). Further, the observed variation in the population ratio for different ground states can then be attributable to the fact that the lower energy K-shell and higher energy L-shell lines are affected most by the opacity.

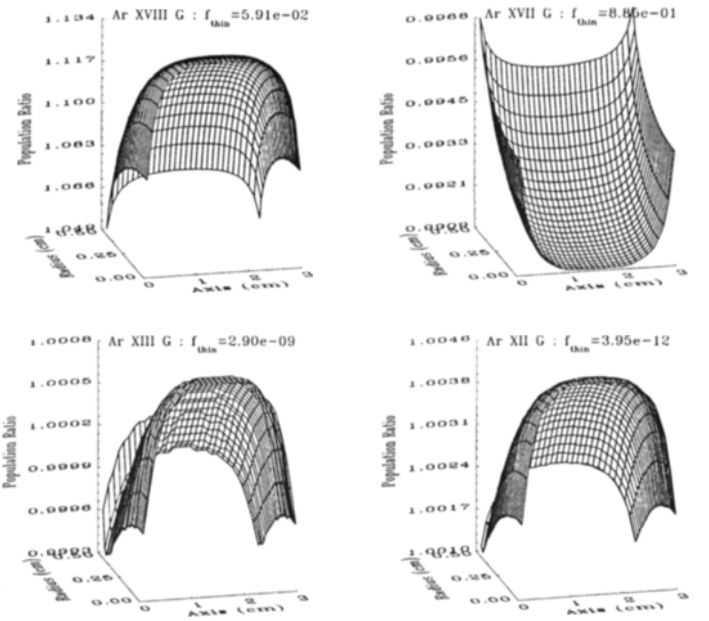

Fig. 4 Atomic population density ratios (thick/thin) for selected ground state ions at 10^{19} ions/cm^3. The corresponding optically thin population density values are noted.

IV Conclusion

We have described a two-dimensional (r,z) time-dependent non-LTE radiation transport and ionization dynamics code, AXSTRAN. The code has the detailed physics and theoretical sophistication to accurately model the non-LTE radiation and ionization dynamics of a multidimensional hot dense plasma throughout its dynamical evolution. An analysis of a uniform argon Z-pinch plasma offered a detailed glimpse at the characteristics of the multidimensional radiation and non-LTE ionization in the plasma. In addition to affecting the local radiation field and ionization distribution, the nonlocal opacity and radiation transport have shown to introduce substantial spatial gradients to the plasma's ionization distribution and to the field itself.

References

1. N. R. Pereira, and J. Davis,J. Appl. Phys. 64, R1 (1988); B. A. Hammel, et al., J. Quant. Spectrosc. Radiat. Transfer 51, 113 (1994).
2. F.L. Cochran and J. Davis, Phys. Fluids B2, 1238 (1990).
3. D. Duston and J. Davis, J. Quant. Spectrosc. Radiat. Transfer 27, 267 (1982).
4. J. W. Thornhill, et al., J. Appl. Phys. 68(1), 33 (1990).
5. D. Mihalas and B. W. Mihalas, *Foundations of Radiation Hydrodynamics*, Oxford Univ. Press, New York, (1984).
6. D. Duston, R. W. Clark, J. Davis, and J. P. Apruzese, Phys. Rev. A27, 1441 (1983).
7. J. B. Sykes, Mon. Not. R. astro. Soc. 111, 377 (1951).
8. Y. K. Chong, et al., to be published in J. Quant. Spectrosc. Radiat. Transfer.